buildings

MDPI

Article

Electrochemical Impedance Spectroscopy Investigation of Accelerated Erosion Mechanisms in Cement-Based Materials Under an Applied Electric Field

Baoxi Zuo [1], Yong Huang [1,*], Yubin Liu [2], Xue Yuan [1], Liran Jiao [1], Hong Wu [1], Sihan Zhang [1] and Ting Liu [1,*]

[1] State Key Laboratory of Chemistry and Utilization of Carbon Based Energy Resources, College of Chemistry, Xinjiang University, Urumqi 830017, China; 13466131731@163.com (B.Z.); 18212100730@163.com (X.Y.); 18799182117@163.com (L.J.); wuhong20233@163.com (H.W.); 17860285327@163.com (S.Z.)

[2] College of Civil Engineering and Architecture, Xinjiang University, Urumqi 830017, China; 18637597005@163.com

* Correspondence: pengyou0991@163.com (Y.H.); liut@xju.edu.cn (T.L.)

Abstract

To address the issues of lengthy test cycles and singular evaluation methods for the durability of cement-based materials in sulfate environments, this study conducted accelerated sulfate erosion experiments on 3D-printed cement-based materials incorporating various supplementary cementitious materials, such as fly ash (FA), silica fume (SF), and metakaolin (MK), by applying a controlled external electric field. Electrochemical impedance spectroscopy (EIS) was employed to characterize the extent of material degradation. By regulating electric field intensity and sulfate solution conditions, and integrating multiple analytical techniques including electrochemical impedance spectroscopy, X-ray diffraction (XRD), scanning electron microscopy (SEM), Fourier-transform infrared spectroscopy (FTIR), and thermogravimetric analysis (TG), this research revealed that the applied electric field accelerates both cement hydration and sulfate-induced degradation through enhanced ion migration. Furthermore, the impedance response characterized by electrochemical impedance spectroscopy showed a positive correlation with macroscopic mechanical properties. Comparative evaluation of sulfate resistance among cement composite systems, FA–cement composites, SF–cement composites, and MK-cement composites indicated that cement-based material with 10% FA addition exhibited the strongest corrosion resistance. This study analyzes the changes in electrochemical impedance spectroscopy characteristic parameters before and after the application of an electric field, systematically elucidating the evolution of the material's microstructure and the patterns of durability degradation. It provides key mechanisms for understanding the durability evolution of cement-based materials exposed to sulfate environments under electric-field assistance, and lays both experimental and theoretical foundations for developing methods to enhance durability.

Keywords: applied electric field; EIS; sulfate attack; durability

Check for updates

Academic Editor: Ray Kai Leung Su

Received: 8 January 2026
Revised: 7 February 2026
Accepted: 9 February 2026
Published: 12 February 2026

Copyright: © 2026 by the authors. Licensee MDPI, Basel, Switzerland. This article is an open access article distributed under the terms and conditions of the Creative Commons Attribution (CC BY) license.

1. Introduction

As a fundamental load-bearing constituent in contemporary construction, the durability of cement-based materials critically influences both the structural integrity and functional longevity of engineered systems [1,2]. Sulfate attack, widely acknowledged as a principal mechanism of concrete degradation, predominantly initiates through the decalcification of calcium silicate hydrate (C-S-H) gel [3–5]. The material's mechanical properties

gradually deteriorate as a result of this process. Conventional methodologies for accelerating deterioration under corrosive conditions, such as full immersion, wet–dry cycling, and partial immersion tests, remain commonly employed [6,7]. Nevertheless, such techniques are often constrained by lengthy experiments and slow degradation kinetics, limiting their use for timely durability assessments. To clarify dissolution-induced damage mechanisms, enhance material performance, and mitigate chemical leaching effects, research has increasingly focused on developing accelerated testing methods [8,9]. Present strategies are broadly classifiable into two main directions: chemically accelerated dissolution employing more aggressive media, typically centered on solutions such as 6 mol/L ammonium nitrate, and electrochemically accelerated dissolution, wherein an external electric field is applied within a deionized aqueous environment to expedite the degradation process [10]. Tasnim, S et al. [11] compared the corrosive effects of water and ammonium nitrate solution on cementitious materials. Their study found that both media induce calcium leaching through similar degradation mechanisms. Quantitatively, however, ammonium nitrate solution was shown to be approximately three hundred times more erosive than water. In a parallel line of inquiry examining the interplay between electric fields and sulfate-induced deterioration, Huanqin Liu et al. [12] proposed accelerating the migration of sulfate ions in concrete by applying an external electric field, thereby enhancing the erosion kinetics. The study systematically examined the effects of parameters such as water-to-cement ratio (0.3–0.5), pulse frequency, curing period (14/28 days), and immersion method on material properties, and validated the sulfate-induced degradation mechanism through microstructural analysis. For 3D-printed cement-based materials formed through layer-by-layer deposition, the process-induced interlayer interfaces and anisotropic structures significantly affect the erosion process, and the mechanisms of supplementary cementitious materials such as FA, SF, and MK in this system also need to be re-evaluated [13]. FA optimizes rheology and extrusion uniformity through its spherical particles and enhances durability through later pozzolanic reactions [14]; SF promotes early hydration, increasing density and erosion resistance through its high reactivity and micro-filling effect [15]; MK improves interfacial bonding and dimensional stability through its alumina-rich phase [16].

EIS provides a nondestructive, real-time, and extremely sensitive in situ monitoring tool for evaluating the durability of cement-based materials by applying low-amplitude alternating current signals and studying the material's electrical response. The method is especially well-suited for clarifying hydration mechanisms and has proven to be an essential tool in durability assessment because of its capacity for long-term, noninvasive tracking of performance progression [17,18]. Illustratively, Madej et al. [19] utilized electrochemical impedance spectroscopy to monitor the hydration kinetics of $SrAl_2O_4$ cement paste, yielding significant data on microstructural development, moisture distribution, and ionic transport throughout the hydration process. Drawing upon conductivity profiles derived from EIS, Bortoletto et al. [20] classified distinct stages of hydration and clarified the associated chemical processes and microstructural evolution within each phase. These studies collectively substantiate that EIS constitutes an effective and dependable methodology for monitoring the hydration kinetics of cementitious materials [21,22]. Furthermore, the ongoing refinement of equivalent circuit modeling has significantly improved the analytical depth with which EIS data can be interpreted. In a representative application, Liu et al. [23] utilized an equivalent electrical circuit (EEC) model to examine the corrosive degradation of cement-based systems exposed to sulfate-laden pore solutions. Their findings demonstrated a measurable correlation between specific circuit parameters and the compressive strength of the materials. Comprehensive investigations have substantiated the capability of EIS to effectively track microstructural transformations in cement-based materials, along with corresponding shifts in their long-term performance and durability [24].

However, the above understanding mainly stems from studies on traditional cast cement-based materials. For emerging 3D-printed cement-based materials, their durability, especially sulfate attack resistance, presents new complexities and research urgency [25]. The inherent layer-by-layer deposition characteristic of this process introduces significant interlayer weak planes, highly anisotropic microstructures, orientation-dependent pores related to the printing path, and unique hydration processes [26]. These process-determined microstructural features are expected to fundamentally alter the transport pathways of corrosive media and reaction kinetics, potentially leading to damage initiation and failure modes markedly different from those of traditional homogeneous concrete [27]. In view of this, directly applying erosion models, accelerated testing methods, and durability evaluation systems established for conventional materials to 3D-printed components faces serious challenges in both scientific validity and reliability [28]. Therefore, this study focuses on 3D-printed cement-based composites, aiming to systematically elucidate the intrinsic relationships among the printing process, anisotropic microstructure, and electrochemical corrosion response, filling the knowledge gap in this field; it also seeks to establish exclusive, rapid, and nondestructive durability assessment methods (such as EIS) suitable for 3D-printed structures, providing key evidence for transitioning from printability to long-term durability.

To achieve these objectives, EIS integrated with equivalent circuit modeling was employed as the principal analytical tool. This investigation systematically examines the hydration and sulfate-induced degradation processes of 3D-printed cementitious composites, specifically FA–cement, SF–cement, and MK–cement systems, under an externally applied electric field. By analyzing the correlation between EIS-derived parameters and compressive strength, along with characterizing the impedance behavior exhibited by each composite under sulfate attack, the role of supplementary cementitious materials in modulating the degradation mechanism was clarified. A systematic relationship between EIS and mechanical performance was established across the studied composites, confirming that the electrical impedance of cement-based materials correlates positively with their macroscopic mechanical properties. This observed interdependence is fundamentally attributed to refined microstructural densification, which concurrently contributes to enhanced mechanical integrity and improved long-term durability. Experimental results under an applied electric field confirmed that electromigration significantly accelerates ionic penetration and associated material degradation. In contrast, the FC10 composite demonstrated superior resistance to such deterioration, attributable to its more refined and stable microstructure. Additionally, by employing an integrated suite of characterization techniques, including XRD, SEM, FTIR, and TG, this work elucidates the electrochemical corrosion mechanisms, delineates microstructural evolution under aggressive environmental conditions, and assesses variations in thermal stability. Collectively, these findings provide a robust scientific foundation for guiding the design and practical application of cement-based materials intended for service in sulfate-laden environments.

2. Materials and Methods

Raw Materials

The materials employed in this study consisted of 42.5 R grade ordinary Portland cement (OPC) produced by Xinjiang Tianshan Cement Co., Ltd., Urumqi, Xinjiang, China, Class I FA sourced from Ganquanbao Industrial Park in Urumqi, Xinjiang, China; high-purity SF supplied by Xinjiang Jingxin Silicon Industry Co., Ltd., Manas County, Xinjiang, China; and MK obtained from Hongyao Mineral Processing Plant in Shijiazhuang, China. Additionally, A polycarboxylate-based high-performance water reducer (PCA-I series) from Jiangsu Sobute New Materials Co., Ltd., Nanjing, Jiangsu, China was used, reducing water

by 25–30%. In this study, DS from the southern Taklimakan Desert was used as the aggregate. The sampling location was a sand quarry situated on the right side of the K8+700 section of the S682 Phase-I project in Segzikule Township, Hotan County, Hotan Prefecture, Xinjiang. The sand had an average particle size of 0.767 mm, a fineness modulus of 0.885, a bulk density of 1647 kg/m^3, an apparent density of 2675 kg/m^3, and a clay content of 1.5%.

The performance of the cement is shown in Table 1. DS, OPC, FA, SF, and MK were analyzed using an X-ray fluorescence spectrometer (XRF), and the chemical composition is shown in Table 2. The five raw materials mainly contain substances such as SiO_2, Fe_2O_3, Al_2O_3, and CaO. The XRD and SEM images of FA, SF, and MK are shown in Figure 1. In the figures, (Figure 1a) FA particles are mostly spherical with rough surfaces, containing numerous micropores and cracks, and irregular shapes; (Figure 1b) SF particles are spherical or quasi-spherical, with visible block-like structures on the surface; (Figure 1c) MK appears in flaky or layered stacks, showing typical honeycomb-like textures on the surface; Figure 1d–f indicate that the three materials mainly contain phases such as SiO_2 and calcium silicate minerals.

Table 1. Properties of ordinary silicate cement.

3D Compressive Strength/MPa	3D Flexural Strength/MPa	Initial Setting Time/min	Final Setting Time/min	Soundness
27.4	5.5	189	257	Qualified

Table 2. The chemical composition of DS, OPC, SF, MK and FA.

	SiO_2	Fe_2O_3	Al_2O_3	CaO	K_2O	MgO	SO_3	TiO_2	Na_2O	P_2O_5
DS	64.79	4.32	13.01	10.64	2.84	2.75	——	0.68	0.77	——
OPC	23.21	5.13	4.76	59.45	0.65	1.25	4.15	0.38	——	——
SF	95.95	0.18	0.91	0.49	0.66	0.46	0.20	——	——	——
MK	49.69	3.03	43.01	0.37	0.29	1.05	0.26	1.88	0.27	——
FA	43.95	11.63	16.25	11.95	1.30	4.12	6.81	0.67	1.55	1.02

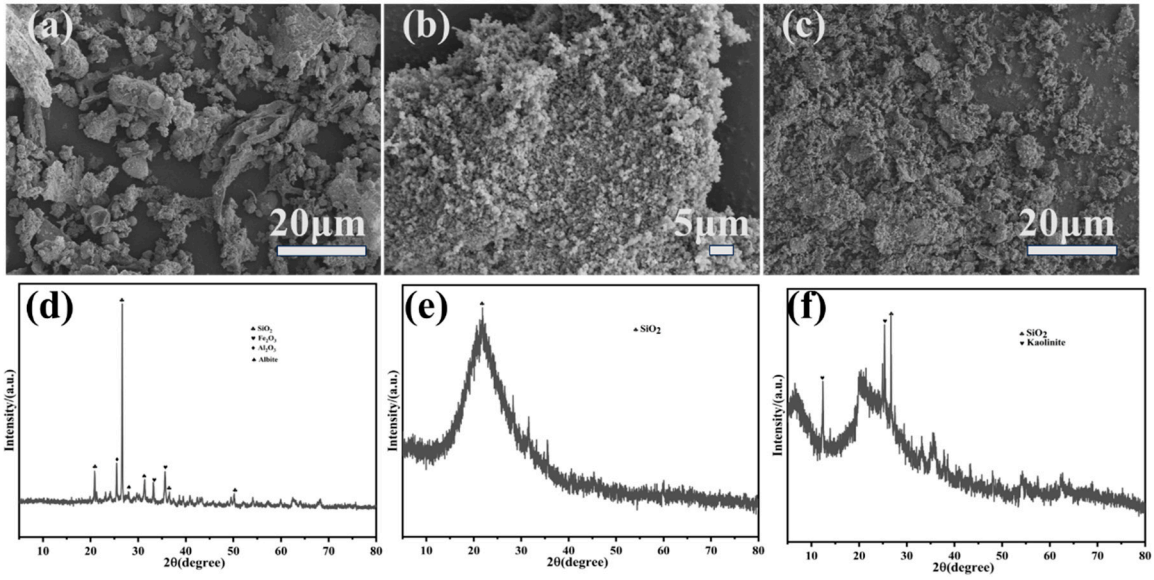

Figure 1. Raw materials: (**a**) SEM of FA, (**b**) SEM of SF, (**c**) SEM of MK, (**d**) XRD of FA, (**e**) XRD of SF, (**f**) XRD of MK.

3. Methods and Design of Experiments

3.1. Designing Experiments and Preparing Specimens

A desktop-scale concrete 3D printing system (Model HC-3DPRT) was utilized in this study, and was manufactured by Hangzhou HC Technology Co., Ltd., Hangzhou, China. As illustrated in Figure 2, the equipment has an overall build volume of 660 mm × 670 mm × 580 mm and incorporates an integrated extrusion unit consisting of a servo motor, material hopper, and screw feeder. The operational parameters were established as follows: a horizontal printing speed of 50 mm/s, a vertical lifting rate of 5 mm/s, and a circular nozzle with a diameter of 30 mm, which served as the standard extrusion component.

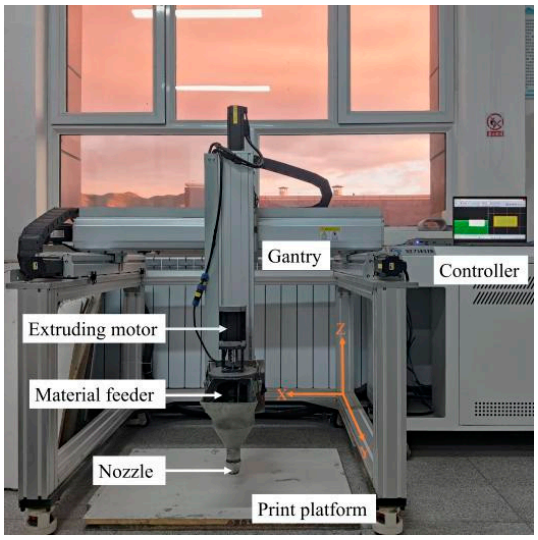

Figure 2. Desktop-level concrete 3D printing system.

Firstly, based on the optimized mix proportion obtained from preliminary pre-experiments, this study systematically investigates the influence of FA, SF, and MK on the printability, mechanical properties, and corrosion resistance of the material. The detailed experimental scheme is presented in Table 3. Four different cementitious material systems were prepared: (i) a pure Portland cement reference group (Control); (ii) a system containing 10% FA (FC10); (iii) a system containing 10% SF (SC10); (iv) a system containing 10% MK (MC10). In all systems, the supplementary cementitious materials were added to the cement at equal mass proportions. A columnar component measuring 360 mm × 200 mm × 150 mm was fabricated via 3D printing, as shown in Figure 3a. The specimen is constructed by continuously extruding a single filament by the print head according to a preset printing path and superimposing it layer by layer. After curing for 24 h, the specimens were maintained under standard environmental conditions (20 ± 2 °C, RH ≥ 95%) for seven days. They were then precisely machined into 40 mm × 40 mm × 160 mm specimens for compressive and flexural strength testing, as illustrated in Figure 3b. All specimens were tested with loading applied along the Z-axis.

Table 3. Mix design of desert sand cement-based materials.

Mix Mode	W/B	Cement/ Kg/m^3	Desert Sand/ Kg/m^3	SP/ Kg/m^3	Water/ Kg/m^3	Fly Ash/ Kg/m^3	Silica Fume/ Kg/m^3	Metakaolin/ Kg/m^3
Control	0.35	635.19	1143.52	13.89	244.44	0	0	0
FC10	0.35	635.19	1143.52	13.89	244.44	63.52	0	0
SC10	0.35	635.19	1143.52	13.89	244.44	0	63.52	0
MC10	0.35	635.19	1143.52	13.89	244.44	0	0	63.52

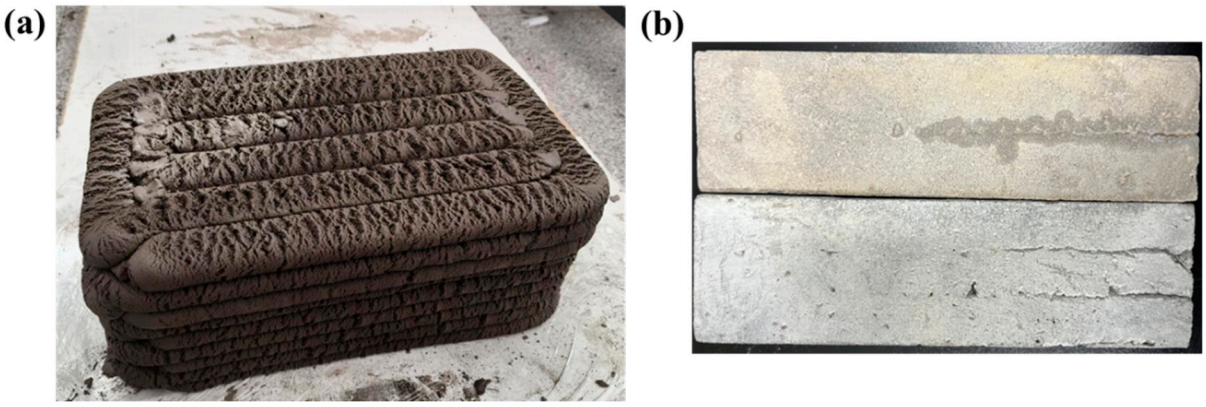

Figure 3. 3D-printed model, (**a**) prismatic member; (**b**) mortar specimen.

3.2. Sulfate Attack Test

Before initiating the erosion resistance assessment, a standardized water saturation protocol was executed employing a BSJ—a fully automated vacuum saturation system. Concrete specimens cured to their specified ages were subjected to comprehensive vacuum saturation using this apparatus. The procedure involved placing the specimens within the vacuum chamber, which was then evacuated and maintained at a controlled vacuum state for one hour. Following this, distilled water was incrementally introduced until complete immersion of the specimens was achieved, after which they remained submerged for three hours. The vacuum condition was persistently maintained for an additional four-hour period prior to re-establishing atmospheric pressure. Subsequently, the specimens underwent further immersion under ambient pressure conditions for eighteen hours to ensure complete saturation.

This study employed two distinct erosion regimes for comparative analysis. The first group of specimens was subjected to free immersion in a 5% Na_2SO_4 solution, while the second group was immersed in an identical solution with the simultaneous application of a constant DC voltage of 30 V. For the electrochemical setup, iridium-coated titanium anodes and titanium cathodes, each with a thickness of 1 mm, were utilized as electrode materials [29]. Every specimen, measuring 40 mm × 40 mm × 160 mm, was kept at a voltage of 30 V. A thermostatic water bath system was used to maintain the temperature at 20 ± 2 °C. Figure 4 shows the matching arrangement of the applied electric field.

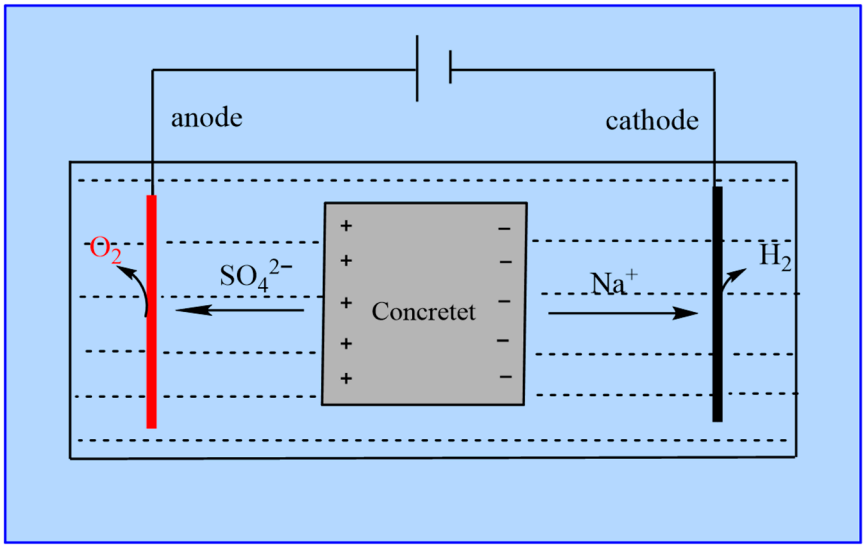

Figure 4. Schematic diagram of the applied electric field.

3.3. EIS Testing Method

EIS measurements were performed using a CHI604E electrochemical analyzer over a frequency range of 0.05 Hz to 100 kHz. Two inert electrodes (stainless steel plates (dimensions: 180 mm × 40 mm × 40 mm; during testing, they are in close contact with the specimen)) along with elastic bands were employed to facilitate impedance acquisition. Specimens subjected to erosion for 0, 7, 14, 21, and 28 days were successively analyzed, with each specimen tested three times to confirm the reproducibility of the experimental results [30,31]. Following impedance measurements, the acquired data were fitted and analyzed using ZView2.exe software. A quasi-Randles equivalent circuit model was established [32], represented as Rs[CPE(RctW)], as illustrated in Figure 5.

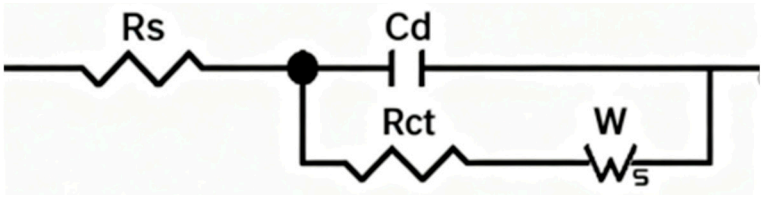

Figure 5. Randles equivalent circuit model for cement-based materials.

3.4. Macroscopic Mechanical Properties Testing

A YAW-SERIES flexural compressive integrated testing machine was used to evaluate the modified cement mortar specimens' flexural and compressive strengths in accordance with the Chinese national standard GB/T 17671-2021 [33].

Procedure for Flexural Testing: The specimen was placed with its longitudinal axis perpendicular to the testing machine's support columns. The loading piston was used to provide a uniformly distributed load at the prism's lateral center at a controlled loading rate of 50 N/s (±10 N/s tolerance) until fracture occurred as depicted in Figure 6a.

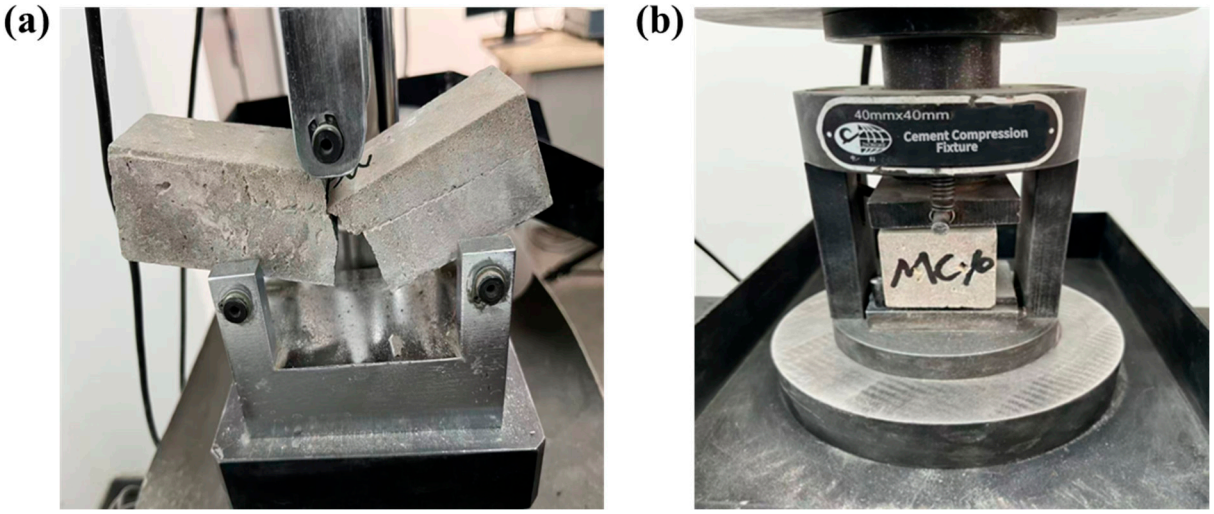

Figure 6. Mechanical Properties Testing: (**a**) Flexural Testing, (**b**) Compressive Testing.

Compressive Testing Procedure: After the flexural test, the two resulting half-prisms were taken out and placed with their broken faces facing down on the testing surface. With each half-prism positioned within ±0.5 mm of the press plate center, around 10 mm of the prism protruded above the plate. Up until failure, a steady loading rate of 2400 ± 200 N/s was applied, and the maximum failure load was noted. The flexural and compressive

strengths were subsequently estimated using Equations (1) and (2), respectively. as depicted in Figure 6b.

$$R_f = \frac{1.5F_f\ L}{b^3} \quad (1)$$

$$R_c = \frac{F_c}{A} \quad (2)$$

"R_f " is the flexural strength (MPa). "F_f " is the load to which the prism's central point was subjected during fracture (N). "L" is the spacing between the supporting cylinders (mm), "b" is the length of the prism's square cross-section. "R_c" is the compressive strength (MPa), "F_c" is the load at the moment of failure (N) and "A" is the loading area (typically 1600 mm^2).

3.5. Materials Characterization

The crystal phases were characterized using XRD (Bruker D8 Advance, Billerica, MA, USA) over a diffraction angle range of 5 to 80 degrees, with a step size of 0.02 and a scanning rate of 10°/min. The test was carried out using Cu-Kα radiation with a working voltage of 40 kV and a current of 40 mA. The morphological characteristics of bone cement-based materials were observed using SEM (Hitachi S4800, Tokyo, Japan) at various magnifications. After vacuum drying, the samples were gold-coated on their fresh fracture surfaces (coating time about 30 s), with an accelerating voltage of 5 kV and a working distance of approximately 10 mm during operation. FTIR spectroscopy (Great 10, Tianjin, China) using the KBr pellet technique was employed to analyze the functional groups in the hydration products. This technique featured a scanning range of 400–4000 cm^{-1} and 32 scans. TG-DTG tests were conducted using the STA 7300 thermogravimetric analyzer (Selb, Germany). The experiments were carried out under a high-purity nitrogen (N_2) atmosphere, with a heating rate of 10 °C/min and a temperature range from 25 °C to 1000 °C.

4. Result and Analysis

4.1. Mechanical Performance Analysis

Four groups of cementitious materials were subjected to 28 days of sulphate immersion and 28 days of accelerated sulphate attack under an applied electric field. Their flexural and compressive strengths were calculated using Equations (1) and (2), with results presented in Figure 7. This figure compares the four groups of cementitious materials after 28 days of natural sulphate immersion and accelerated corrosion under an applied electric field, revealing systematic changes in both compressive and flexural strengths. The comparison indicates that specimens subjected to the electric field exhibited significantly lower mechanical properties than those undergoing natural corrosion over the same period. This phenomenon is attributed to the intense electromigration effect induced by the applied electric field. This effect drives the directional and rapid migration of corrosive ions such as SO_4^{2-} within the material matrix [34]. This not only intensifies the chemical dissolution of hydration products (CH, C-S-H gel) but also accelerates the formation and accumulation of expansive products like ettringite (AFt) and gypsum. The resulting crystallization pressure induces microcrack propagation from within, compromising structural integrity and manifesting macroscopically as accelerated deterioration in compressive and flexural strength [35].

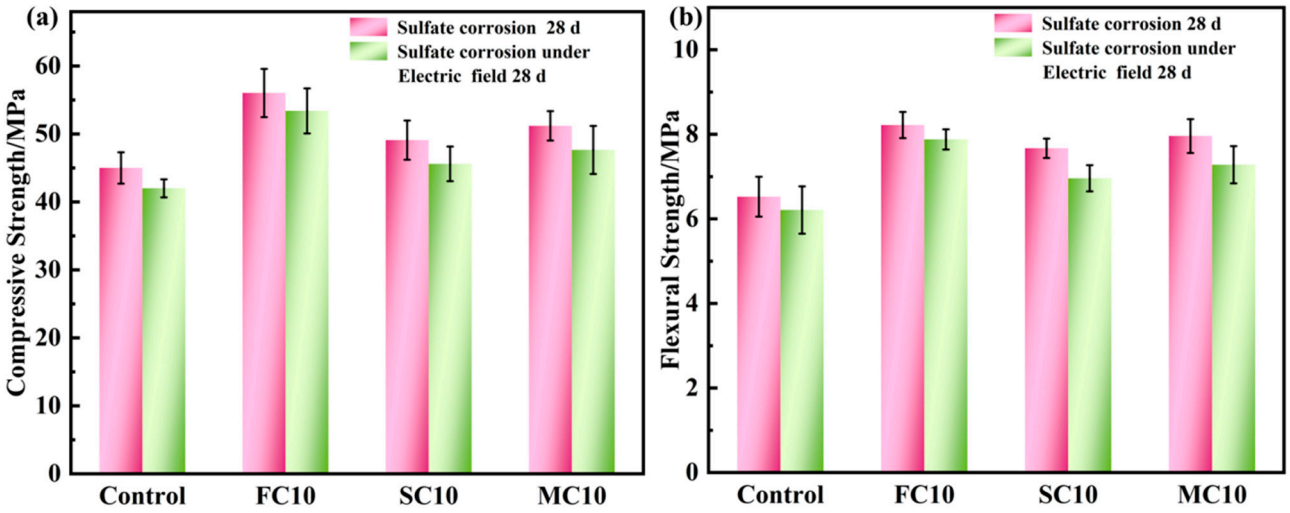

Figure 7. Mechanical performance of specimens after 0 d, 28 d sulfate exposure, and 28 d electric field-accelerated sulfate exposure: (**a**) compressive strength; (**b**) flexural strength.

4.2. EIS Analysis

EIS was employed to analyze the corrosion process of cementitious materials in a sulphate environment. Figure 8 compares the Nyquist plots of four specimen groups after 28 days of natural corrosion in a 5% Na_2SO_4 solution and after 28 days of corrosion under an applied electric field. The results demonstrate that the capacitive arc radius of specimens subjected to an electric field is significantly smaller than that of naturally corroded specimens, indicating reduced material resistance and accelerated corrosion. This phenomenon directly corroborates that the applied electric field, through a pronounced electromigration effect, significantly enhances the transport rate and penetration depth of corrosive ions such as SO_4^{2-} [36]. The intensified ion migration accelerates the electrochemical reaction between sulphates and hydration products, promoting the formation and accumulation of expansive products. At the microscopic level, the crystallization pressure from expansion induces microcrack propagation, compromising the material's compactness and integrity. This electrically driven corrosion process manifests in EIS as a reduction in the capacitive arc radius [18], fundamentally reflecting direct microstructural damage within the material. Such damage inevitably leads to a decline in macroscopic mechanical properties. Consequently, the diminishing capacitive arc radius serves as an effective electrochemical indicator for predicting and explaining the macroscopic performance degradation of cementitious materials under the coupled action of electric fields and sulphates.

Figure 9a–c illustrate the evolution of Nyquist plots for FC10, SC10 and MC10 materials under sulphate attack with an applied electric field from 14 to 42 days. The plots reveal that the capacitive arc radius for all three specimens first increases then decreases, reflecting a dynamic process where the materials undergo initial densification followed by deterioration under the electric field. During the periods from 14 to 28 days (FC10) and 14 to 35 days (SC10, MC10), the capacitive arc radius continuously increased, indicating the materials were in an electrochemical densification phase. In this stage, the products of sustained hydration reactions effectively filled pores, refined pore size, and enhanced overall impedance and permeability resistance [37], analogous to the electrochemical curing effect. However, beyond 28 days (FC10) and 35 days (SC10, MC10), the capacitive arc radius begins to decrease, indicating that sulphate erosion effects have surpassed the self-compaction process. Upon accumulation of erosive ions to critical concentrations, expansion products form and gel dissolution occurs, leading to microcrack propagation and structural damage, which cause deterioration in electrical resistance and durability [38].

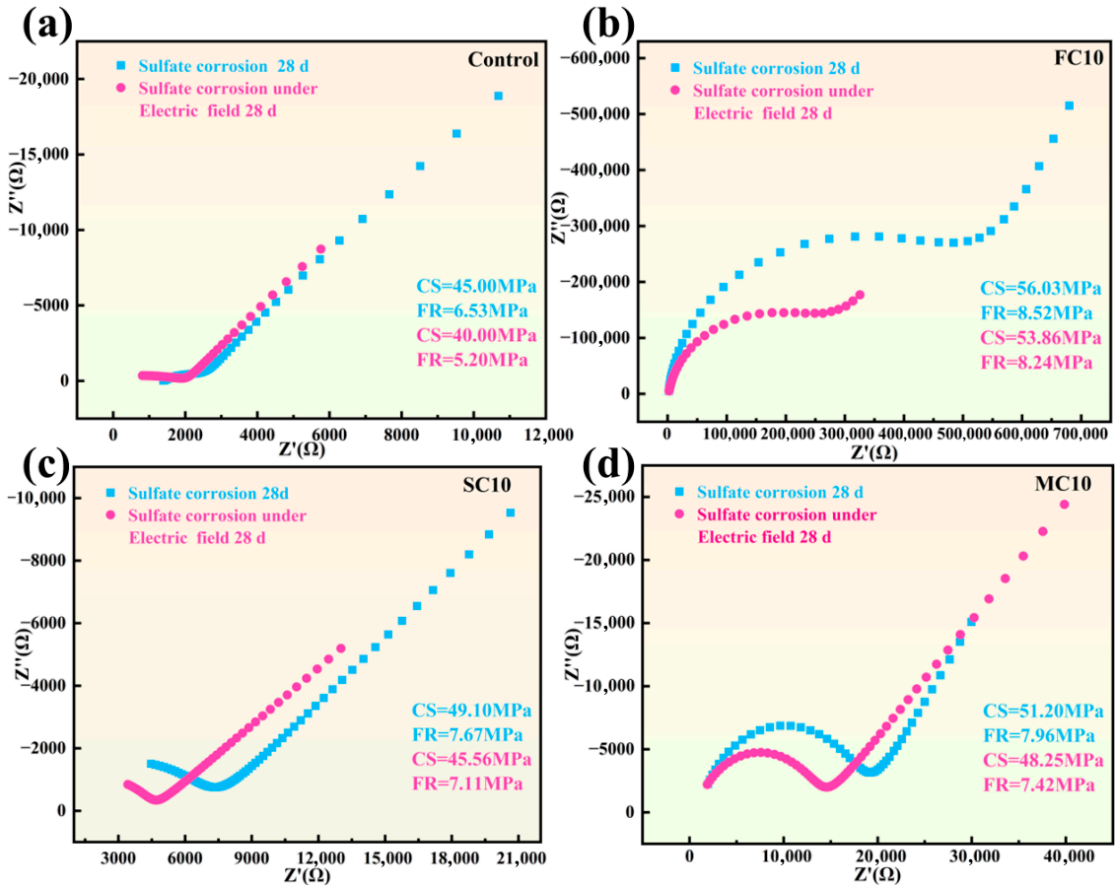

Figure 8. Nyquist diagram after 28 d sulfate immersion and 28 d electric field-accelerated sulfate exposure. (**a**–**d**) correspond to the Control group, FC10 group, SC10 group, and MC10 group, respectively.

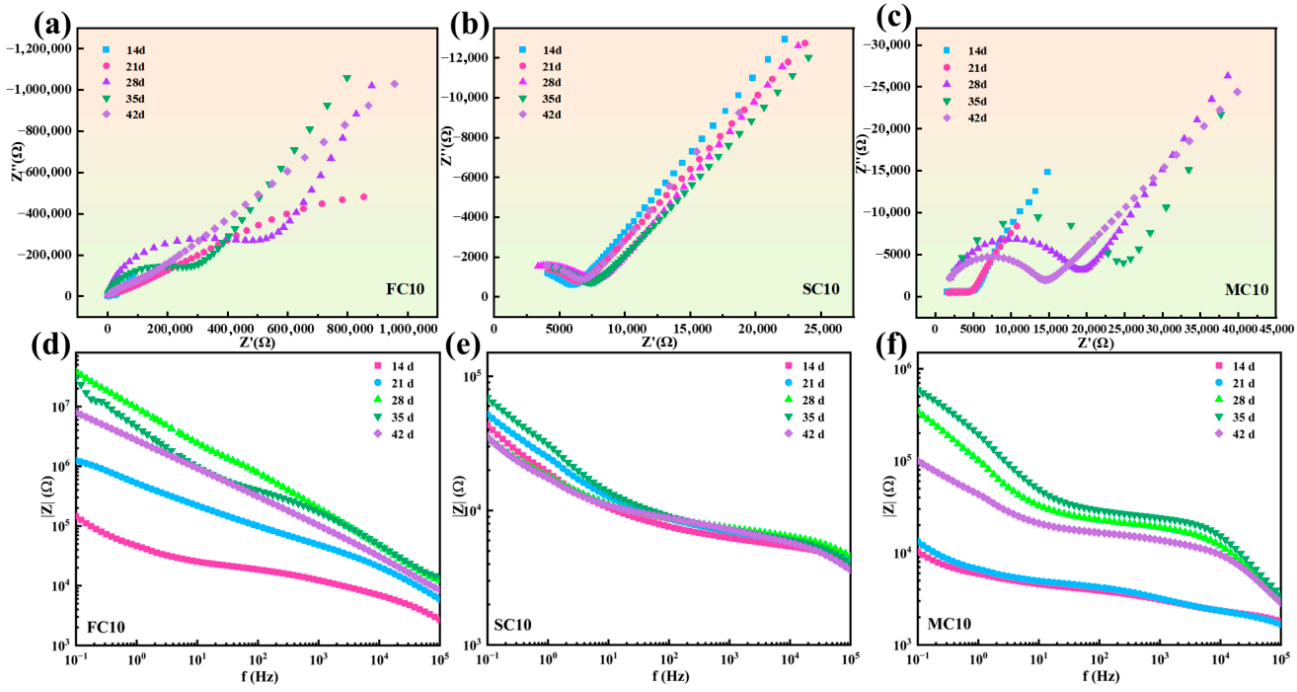

Figure 9. Nyquist diagram and Bode plots of sulfate corrosion under applied electric field at 14–42 days, (**a**–**c**) present the Nyquist diagram of the FC10, SC10, and MC10 groups, respectively; (**d**–**f**) display the Bode diagrams corresponding to the FC10, SC10, and MC10 groups, respectively.

The Bode plots in Figure 9d–f further corroborate the aforementioned conclusions. The FC10 group exhibited the highest impedance modulus at 28 days, indicating its most compact microstructure and optimal corrosion resistance [39]. The SC10 and MC10 groups reached their maximum modulus values at 35 days, indicating the formation of relatively stable structures at this stage with enhanced erosion resistance. The EIS results align with the Bode plots, collectively revealing the time-dependent evolution patterns of different admixture systems under the coupled effects of electric field and sulphate.

Figure 10 compares the EIS spectra of four cementitious materials after 7 and 28 days of sulphate corrosion under an applied electric field, alongside their corresponding mechanical properties and pore resistivity. Results indicate that the capacitive arc radius, compressive strength, and flexural strength of all materials follow the pattern: FC10 > MC10 > SC10 > Control. The FC10 group exhibited the largest capacitive arc radius at all aging periods, indicating superior resistance to ion migration and medium permeation, alongside the most compact and stable microstructure. This outstanding performance is attributed to the pozzolanic effect of FA, which optimizes the composition of hydration products, refines pore size, and enhances pore tortuosity, thereby forming a highly dense microstructure [40]. This structure effectively impedes the diffusion of corrosive media such as SO_4^{2-}, water, and oxygen, manifesting macroscopically as enhanced impedance and mechanical properties [41]. The high consistency between EIS and macroscopic mechanical properties validates the efficacy of electrochemical impedance as a durability evaluation metric.

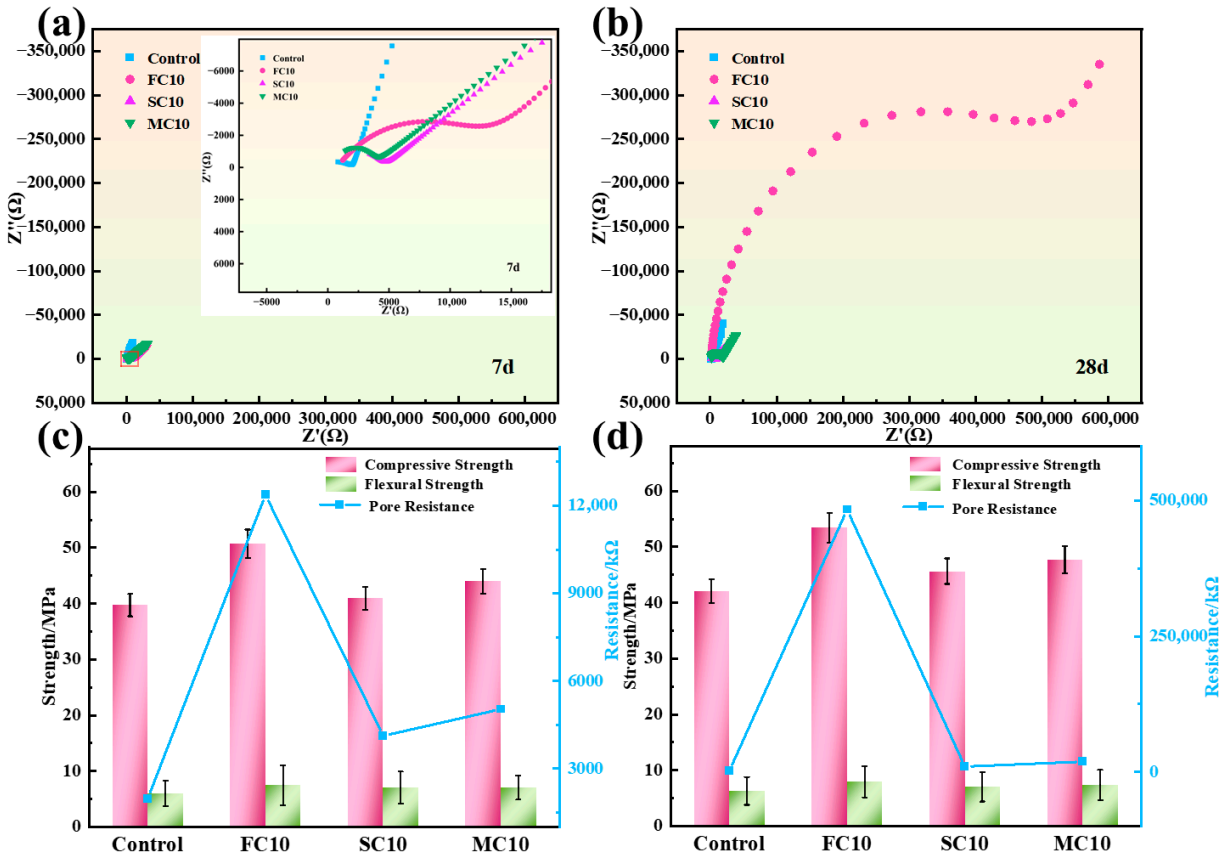

Figure 10. (**a**) show the Nyquist diagram of sulfate corrosion under applied electric field at 7 days, (**b**) show the Nyquist diagram of sulfate corrosion under applied electric field at 28 days, (**c**) illustrate the compressive strength, flexural strength, and pore resistance corresponding to sulfate corrosion under applied electric field at 7 days, (**d**) illustrate the compressive strength, flexural strength, and pore resistance corresponding to sulfate corrosion under applied electric field at 28 days.

4.3. XRD Analysis

To investigate the effects of sulphate attack on cement hydration products, XRD testing was conducted on the specimens. Figure 11 presents the XRD patterns of four cementitious materials after 28 days of attack, with primary phases including quartz (SiO_2), $Ca(OH)_2$, C-(A)-S-H, C_3S, and AFt [42]. The pronounced quartz peak originates from unreacted components in the raw materials. Comparative analysis reveals that specimens subjected to 28 days of conventional sulphate attack exhibit higher peak intensities for $Ca(OH)_2$, C_3S, and C-(A)-S-H than those exposed to the same duration of attack under an applied electric field. This indicates that the electric field intensifies ion migration and corrosion reactions, accelerating the decomposition of hydration products. Under varying corrosion conditions, the characteristic peak intensities of the FC10 group consistently exceeded those of the control group, indicating that its mix design fosters a more stable and corrosion-resistant microstructure. This is primarily attributed to the synergistic densification effect of optimized particle grading and pozzolanic reaction. This effectively inhibits the migration and penetration of SO_4^{2-} driven by the electric field, retarding the reaction with $Ca(OH)_2$ to form products such as gypsum [43,44], thereby better preserving the calcium hydroxide phase. This result confirms that the FC10 group exhibits optimal resistance to ion migration and chemical erosion, consistent with its superior performance in macroscopic mechanical properties, microstructure morphology, and EIS.

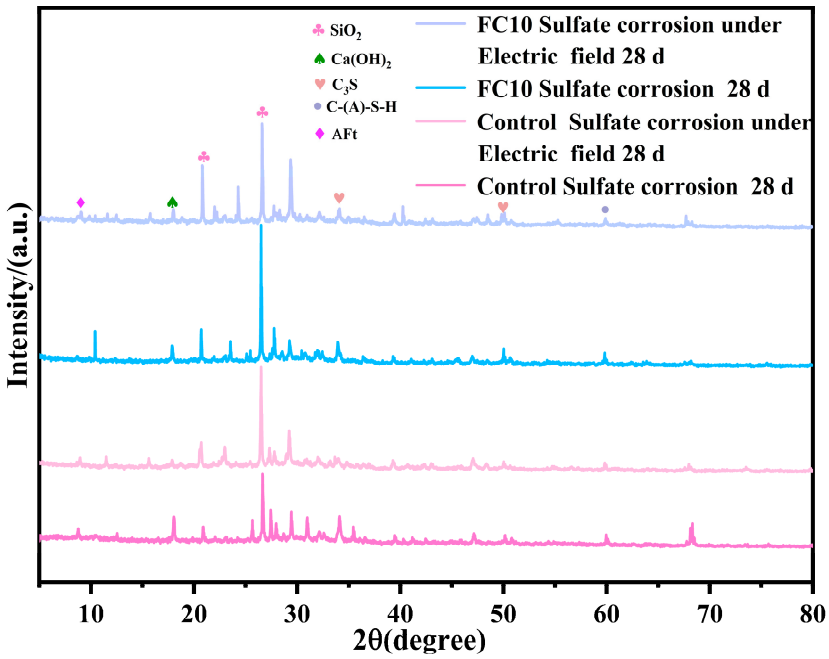

Figure 11. XRD of cement-based materials after 28 d sulfate immersion and 28 d electric-field-accelerated sulfate exposure.

4.4. SEM Analysis

Figure 12 compares the microstructural evolution of four cementitious materials before and after corrosion via SEM analysis. Prior to corrosion (Figure 12a–d), all specimens exhibited a dense structure. Numerous gel-like hydration products and acicular AFt particles are visible, with low porosity indicating thorough initial hydration reactions. This formed an effective pore-filling system dominated by C-S-H gel and $Ca(OH)_2$, providing the material with good initial strength and compactness.

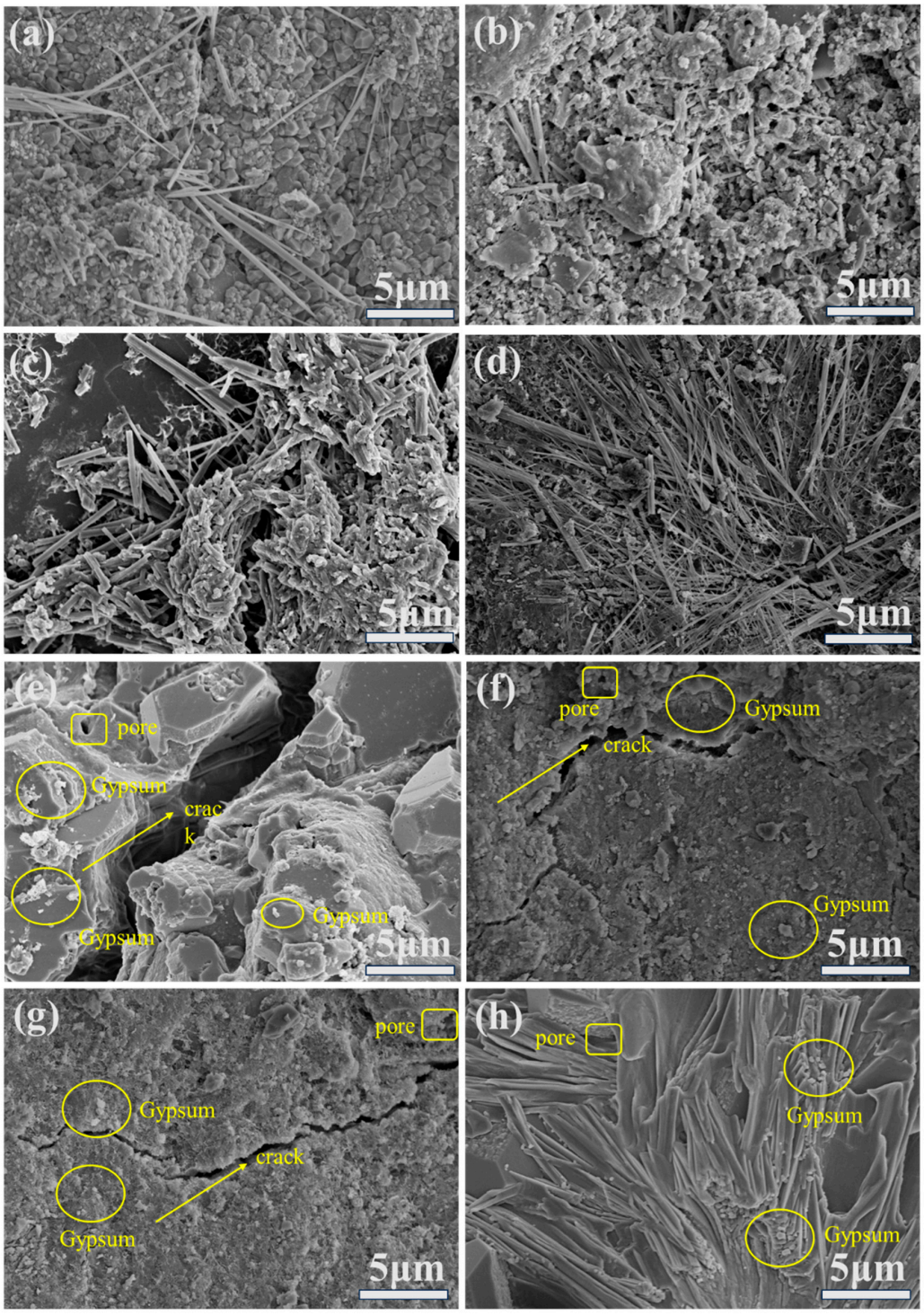

Figure 12. SEM micrographs of the specimens showing the corrosion process: (**a**–**d**) show the pre-exposure control, FC10, SC10 and MC10 specimens, respectively; (**e**–**h**) show the post-exposure control, FC10, SC10 and MC10 specimens, respectively.

Following 28 days of corrosion by a 5% Na_2SO_4 solution under an applied electric field (Figure 12e–h), the microstructure exhibited significant deterioration. The number of AFt particles decreased across all groups. The Control group (Figure 12e) displayed pronounced large-scale cracks, followed by FC10 (Figure 12f) and SC10 (Figure 12g). In contrast, the MC10 group (Figure 12h) showed no major cracks, instead forming an interwoven network structure. The corrosion also induced copious plate-like and granular products, accompanied by the formation of pores and cavities. This indicates decalcification of the

C-S-H gel and silicate leaching, leading to the generation of non-gel-phase calcium silicate. These morphological alterations reflect typical characteristics of sulphate attack: crack propagation, gel wrinkling deformation, structural loosening, and pore evolution. The attack mechanism primarily involves the formation reactions of expansive products such as gypsum (Equations (3)–(7)) [32,45], which, under the influence of an electric field, accelerate ion migration and product accumulation, thereby intensifying microstructural degradation.

$$2Na^+ + SO_4^{2-} + 10H_2O \rightarrow Na_2SO_4 \cdot 10H_2O \quad (3)$$

$$CH + SO_4^{2-} + 2H \rightarrow 3C\bar{S}H_2 + 2OH^- \quad (4)$$

$$C_3A + 3C\bar{S}H_2 + 26H \rightarrow C_6A\bar{S}_3H_{32} \quad (5)$$

$$C_4AH_{13} + 3C\bar{S}H_2 + 14H \rightarrow C_6A\bar{S}_3H_{32} + CH \quad (6)$$

$$C_4A\bar{S}H_{12} + 2C\bar{S}H_2 + 16H \rightarrow C_6A\bar{S}_3H_{32} \quad (7)$$

4.5. FTIR Analysis

FTIR spectra were acquired for four groups of cementitious materials before and after corrosion, as shown in Figure 13. Figure 13a indicates that the types of hydration products in each sample were similar prior to corrosion, though differences in spectral wavenumbers were observed, reflecting subtle variations in composition and structure. The peak at 3458.4 cm^{-1} corresponds to the O-H stretching vibration, primarily attributed to bound water and hydroxyl groups within the C-(A)-S-H gel; 1597.2 cm^{-1} corresponds to the H-O-H bending vibration peak; and the region around 1360 cm^{-1} represents the O-C-O asymmetric stretching vibration peak of carbonate ions, originating from the carbonate content in the raw materials and carbonation processes [46,47]. Figure 13b presents the FTIR spectrum after 28 days of sulphate corrosion under an applied electric field. Compared to the pre-corrosion state, the intensity and area of the O-H peak at 3458.4 cm^{-1} significantly increased, indicating continuous accumulation of quartz phases. This is primarily attributed to the high crystalline water content in the calcium aluminate hydrate. Concurrently, the characteristic quartz peak at 774.8 cm^{-1} disappeared, resulting from microstructural disruption and compositional changes caused by SO_4^{2-} reacting with the hydration products.

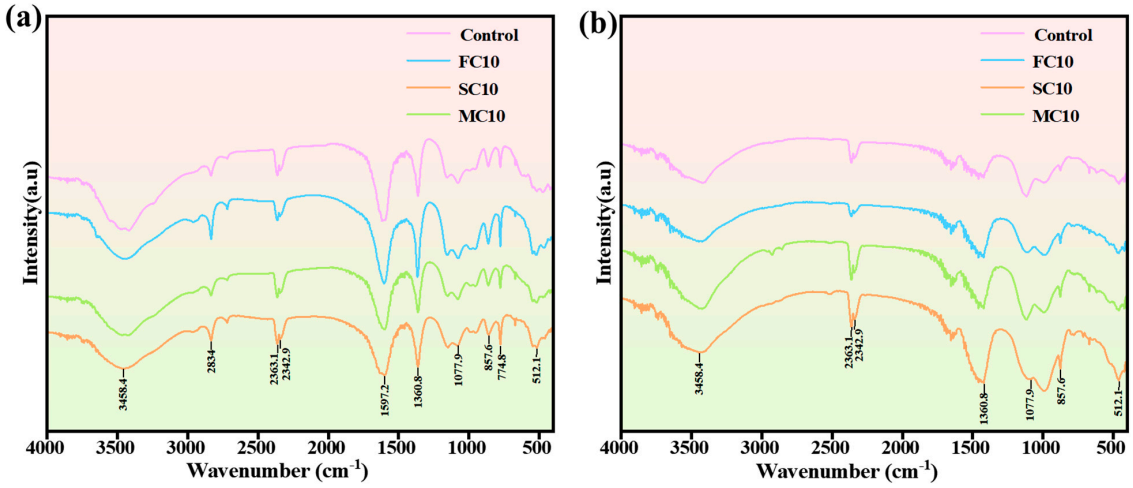

Figure 13. FTIR spectra of the four cement-based material groups: (**a**) Control, FC10, SC10, and MC10 before corrosion (0 d); (**b**) Control, FC10, SC10, and MC10 after 28 d of electric-field-accelerated sulfate attack.

Comparative analysis further revealed that post-corrosion $Ca(OH)_2$ and C-S-H characteristic peak intensities exhibited a marked reduction, indicating that sulphate attack led to the decomposition of hydration products. The mineral admixture-containing FC10, SC10, and MC10 mixtures effectively consumed $Ca(OH)_2$ through pozzolanic reactions, converting it into a C-S-H gel with a lower calcium-to-silica ratio and enhanced stability, thereby improving their corrosion resistance [47,48]. Among these, the FC10 group exhibited the highest pozzolanic activity, with its $Ca(OH)_2$ peak nearly disappearing. The Si-O and Si-O-Si vibration peaks showed high intensity and increased polymerization, indicating the fastest formation of a high-density, low-permeability structure. This effectively delays ion intrusion and demonstrates the greatest potential for long-term durability.

4.6. TG Analysis

The thermal decomposition behavior of cement hydration products is directly correlated with their phase composition, with distinct decomposition temperature ranges characteristic of different products. TG analysis effectively characterizes the influence of various additions on hydration product composition. As shown in Figure 14, the pyrolysis process of cementitious materials can be divided into three stages: the 70–200 °C range primarily involves free water evaporation and dehydration of hydration products such as C-S-H gel and AFt; the 350–550 °C range corresponds to the decomposition reaction of $Ca(OH)_2$; the 600–750 °C range is attributed to the high-temperature decomposition of the carbonation product $CaCO_3$ [49,50], with the relevant reaction equations shown in Equations (8)–(10).

$$Ca(OH)_2 \triangleq CaO + H_2O \quad (8)$$

$$CaO + CO_2 = CaCO_3 \quad (9)$$

$$CaCO_3 \triangleq CO_2 + CaO \quad (10)$$

Comparing the TG-DTG curves of un-eroded specimens with those subjected to electric field-sulphate erosion, as shown in Figure 14, reveals distinct alterations in the composition and content of hydration products. Characteristic peak intensities within the DTG curve of eroded specimens exhibit changes, primarily attributable to the depletion and transformation of initial hydration phases. Between 70 and 200 °C, the dehydration peak intensities of C-S-H gel and AFt markedly diminish, indicating gradual depletion of the primary cementitious phases within the matrix due to their participation in degradation reactions (Equations (11) and (12)) induced by sulphate attack. Between 350 and 550 °C, the intensity of the endothermic peak corresponding to $Ca(OH)_2$ decreased. This resulted from the reaction between SO_2 and CH to form gypsum dihydrate (Equation (11)), which not only reduced the system's alkalinity but also signaled that the erosion could profoundly influence the composition of the hydration products [51,52]. Between 600 and 750 °C, the intensity variations in the first three $CaCO_3$ decomposition peaks intensify. This arises from microcracks induced by erosion accelerating carbonation reactions, generating decomposable products such as carbon–sulphur–silicate–calcite, whose signals overlap with the $CaCO_3$ peak. Conversely, the attenuation of the $CaCO_3$ peak in MC10 stems from sulphate erosion consuming substantial calcium sources for gypsum formation, thereby reducing available Ca^{2+} for carbonation and inhibiting calcium carbonate formation [53].

$$Ca(OH)_2 + {SO_4}^{2-} + 2H_2O \rightarrow CaSO_4 \cdot 2H_2O + 2OH^- \quad (11)$$

$$\text{C-S-H} + {SO_4}^{2-} \rightarrow \text{C-S-H} + CaSO_4 \cdot 2H_2O \quad (12)$$

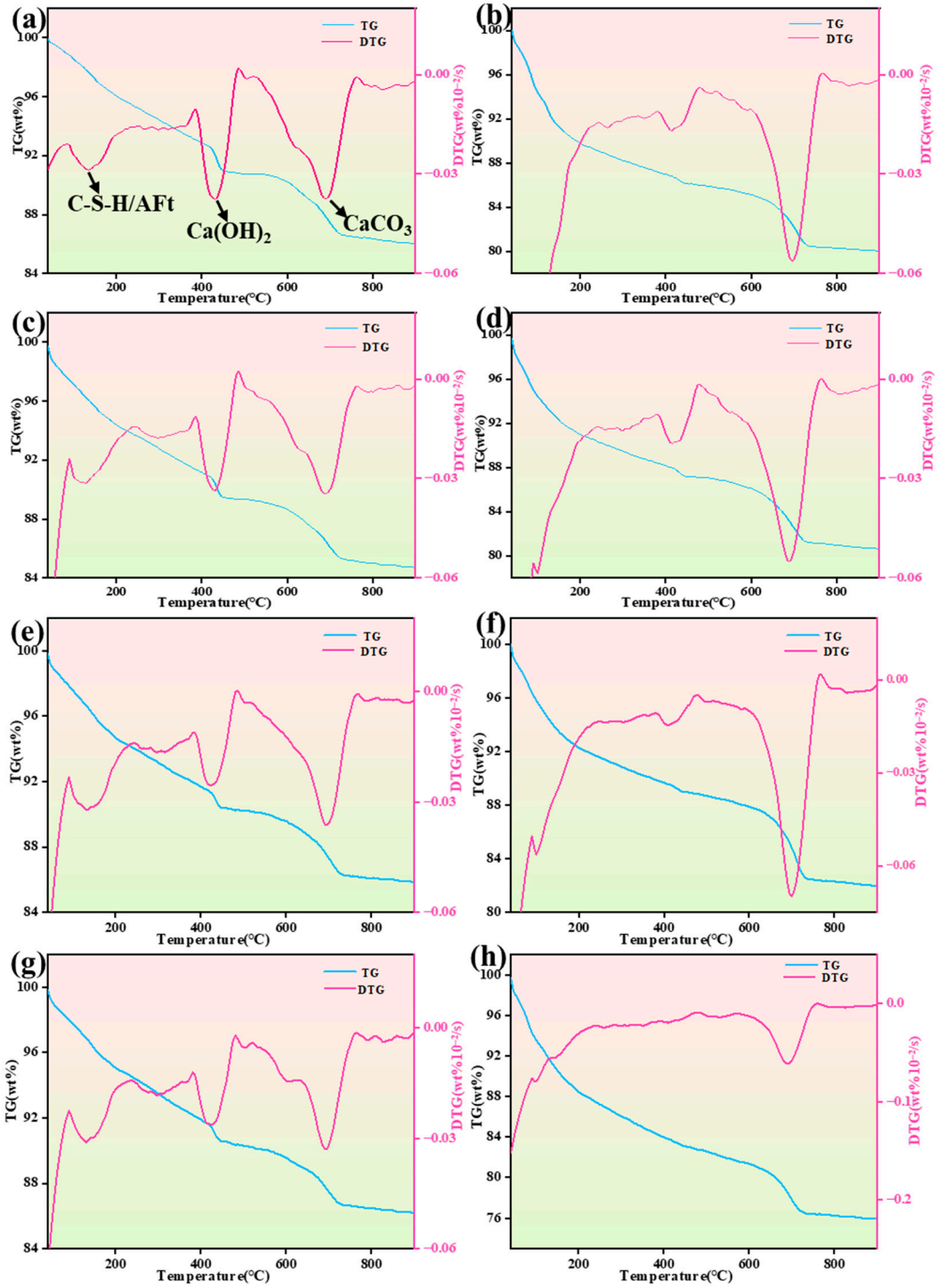

Figure 14. (**a**,**b**) TG and DTG curves of the Control group before and after electric-field-accelerated sulfate exposure; (**c**,**d**) TG and DTG curves of the FC10 group before and after electric-field-accelerated sulfate exposure; (**e**,**f**) TG and DTG curves of the SC10 group before and after electric-field-accelerated sulfate exposure; (**g**,**h**) TG and DTG curves of the MC10 group before and after electric-field-accelerated sulfate exposure.

4.7. The Correlation Between Acceleration Conditions and Actual Usage Environments

The fundamental purpose of this method (electric-field-assisted) is mechanism research rather than precise lifespan prediction. Its core value lies in the fact that sulfate ion migration driven by the electric field and natural diffusion are similar in terms of the physical nature of transport and the chemical reaction products. Therefore, the electric

field acceleration mainly changes the kinetics without altering the degradation mechanism (such as the formation of gypsum and ettringite), making the microstructural evolution and performance deterioration trends observed under accelerated conditions highly valuable for understanding long-term degradation patterns in actual environments. Based on this, this study effectively distinguished and qualitatively ranked the corrosion resistance of different 3D printing mixtures (FA, SF, MK) through electric-field-accelerated tests. For example, systems that perform better under accelerated conditions (such as FC10) can be inferred to have better durability potential under long-term natural exposure, providing a powerful tool for material selection. This correlation also offers key optimization directions for designing 3D-printed cement-based materials for harsh environments (such as sulfate-rich underground or marine splash zones). For instance, the FC10 system, due to its dense microstructure and excellent resistance observed in accelerated tests, can be considered a preferred candidate material for such applications.

4.8. Limitations and Prospects of Research Methodology

The electric-field-assisted method used in this study accelerates the erosion process by driving ion migration, and its core value lies in mechanistic research and qualitative sequencing of material systems, rather than providing accurate long-term life prediction. However, the applied electric field will introduce physicochemical effects that do not exist under natural diffusion conditions; for example, the direct current field may trigger the electrolytic reaction and Joule heat, which in turn interferes with the pH value of the pore liquid and the local temperature field. At the same time, the directional migration of ions caused by constant electric fields is also different from the multidimensional diffusion under natural conditions, which may affect the spatial distribution of erosion products. Although the off-target effects were suppressed by measures such as lower current density (937.5 A/m^2) and the consistency of the degradation mechanism was confirmed, there were inherent uncertainties in extrapolating the acceleration results to the actual environment. On the one hand, the electric field mainly accelerates ion transport, and the degree of acceleration of chemical reaction steps may be different, which makes it difficult to establish a universal quantitative acceleration coefficient. On the other hand, the actual environment is usually coupled with multiple factors such as the dry–wet cycle, freeze–thaw, chloride ion erosion and load, while this test only focuses on a single sulfate erosion process. Therefore, the conclusions of this study should be used as a key basis for material screening; for example, the FC10 system, which performs better under accelerated conditions, shows the potential for better long-term performance, but its practical engineering application still needs to be further verified by multi-factor coupled durability tests that are closer to reality.

5. Conclusions

This study systematically evaluated cement-based composites with varying proportions of FA, SF, and MK through compressive and flexural strength tests, electric-field-accelerated sulfate corrosion, XRD, SEM, and TG analyses. The primary conclusions of this study are summarized below:

(1) There is a clear correlation between the electrochemical impedance characteristics and macroscopic mechanical performance of cement-based materials. In particular, increased electrical resistance reflects a more compact microstructure and reduced porosity. This refined microstructure not only effectively limits the penetration of deleterious species, thereby improving corrosion resistance, but also strengthens the load-carrying ability of the matrix, leading to higher compressive and flexural strengths.

(2) The external electric field generates a strong electromigration effect that directs and accelerates the transport of aggressive ions through the cement-based matrix. This accelerates both the chemical degradation of hydration products and the precipitation of expansive secondary phases, thereby promoting internal microcracking and structural damage that propagates outward.
(3) Among the four cement-based systems examined, the FC10 composite demonstrated superior mechanical properties, including enhanced compressive and flexural strengths, compared to the other formulations. Additionally, it exhibited the highest durability performance across varied corrosive environments. Overall, the FC10 formulation displays the most optimal comprehensive performance.

This study established a new durability evaluation framework for 3D-printed cement-based materials with heterogeneous and anisotropic structures by integrating electric field acceleration with in situ monitoring using EIS. Traditional acceleration methods are based on the assumption of material homogeneity, making them difficult to apply to printed structures with interlayer interfaces and oriented pores. By coupling electric field acceleration with EIS technology, this study achieved spatiotemporal tracking of ion migration, interfacial reactions, and microstructural evolution during the erosion process, clarifying the applicability limits of this method in printed systems and providing a basis for developing dedicated accelerated testing standards for additive manufacturing structures.

At the same time, this study established a multi-scale, multi-signal synergistic evaluation system, clarifying the influence of anisotropic structures on erosion mechanisms and deepening the understanding of the damage mechanisms of 3D-printed materials under the coupled effects of chemical and electric fields. The related findings provide theoretical guidance for regulating printing parameters, optimizing material rheology, and enhancing interfacial performance, promoting the advancement of this field from phenomenological observation to mechanistic regulation. The proposed combined electric field–EIS–microstructure method can serve as a high-throughput screening tool for material development and lays the foundation for establishing durability evaluation standards based on structural performance in the future.

Author Contributions: Methodology, B.Z., X.Y., L.J. and T.L.; Validation, B.Z., Y.L., H.W. and S.Z.; Resources, Y.H.; Data curation, Y.H.; Writing—original draft, B.Z. and H.W.; Writing—review and editing, Y.L., X.Y., L.J., S.Z. and T.L.; Supervision, T.L. All authors have read and agreed to the published version of the manuscript.

Funding: This research was funded by the 2024 Autonomous Region Third Batch "Tianshan Talents" Training Program Project: Desert Sand Composite Industrial Solid Waste Green Low-Carbon Engineering Materials Innovation Team (Grant No. 2024TSYCTD0001); the 2023 Xinjiang Uygur Autonomous Region Key R&D Program Project: Key Technologies for Mine Eco-geological Environment Restoration and Green Low-Carbon Comprehensive Recycling of Iron Ore Tailings (Grant No. 2023B03011-3); the Major Science and Technology Project of Xinjiang Production and Construction Corps titled "Research and Demonstration of Complete Technologies for Concrete and Intelligent Management and Control Resistant to Complex Saline-Alkali Environments in Southern Xinjiang" [No. 2024AA007], the Key Field Science and Technology Research Project of Xinjiang Production and Construction Corps titled "Research and Industrialization Demonstration of Complete Technology for In situ Material-Based Green and Low-Carbon Highway Mobile 3D Printing Construction" [No. 2025AB019], and the Project of Xinjiang Department of Industry and Information Technology titled "Research and Demonstration of Complete Technology for In situ Material-Based Green, Environmentally Friendly, Low-Cost Plateau Mining Road Construction Using Mobile 3D Printing".

Data Availability Statement: The data presented in this study are available in the article.

Conflicts of Interest: The authors declare no conflicts of interest.

References

1. Liu, H.; Yang, X.; Jiang, L.; Li, K.; Wang, L.; Jin, W. Study on the Effect of Interfacial Modification on the Properties of Super Standard Mica Sand Cement-Based Materials. *Buildings* **2024**, *14*, 1665. [CrossRef]
2. Ma, J.; Yang, Q.; Peng, X.; Xia, K. Review on Durability Deterioration and Mitigation of Concrete Structures. *Coatings* **2025**, *15*, 982. [CrossRef]
3. Wang, D.; Zhang, G.; Ding, Q.; Yan, P.; Li, Y. Microstructural evolution and degradation mechanisms of tricalcium silicate and tricalcium aluminate composite pastes under sulfate exposure. *Case Stud. Constr. Mater.* **2024**, *21*, e04050. [CrossRef]
4. Zhao, Y.; Wang, L.; Zeng, L.; Jiang, X.; Zhou, K. Avalanches in concrete compression failure under sulfate attack. *Mater. Struct.* **2022**, *55*, 249. [CrossRef]
5. Belghali, M.; Ayed, K.; Ezziane, M.; Leklou, N. The influence of sulfate attack on existing concrete bridges: Study of external sulfate attack (ESA). *Constr. Build. Mater.* **2025**, *483*, 141751. [CrossRef]
6. Zhang, M.; Zou, D.; Qin, S.; Zhang, X.; Liu, T. Decoupling chemical and physical sulfate attack on OPC and L.SAC concrete under wet-dry cycles. *J. Build. Eng.* **2024**, *99*, 111637. [CrossRef]
7. Chong, L.; Yang, J.; Chang, J.; Aierken, A.; Liu, H.; Liang, C.; Tan, D. Corrosion Behavior of Magnesium Potassium Phosphate Cement under Wet-Dry Cycle and Sulfate Attack. *Materials* **2023**, *16*, 1101. [CrossRef]
8. Alyami, M.H.; Alrashidi, R.S.; Mosavi, H.; Almarshoud, M.A.; Riding, K.A. Potential accelerated test methods for physical sulfate attack on concrete. *Constr. Build. Mater.* **2019**, *229*, 116920. [CrossRef]
9. Nguyen, V.-H.; Leklou, N.; Mounanga, P. Development of accelerated test methods by electromigration to assess the risk of internal sulfate attack in heat-cured mortar and concrete. *Constr. Build. Mater.* **2024**, *455*, 139185. [CrossRef]
10. Mao, L.-X.; Li, L.-Y.; Kim, B. Modelling of multi-species transport in concrete under the action of external electric field: Influence of the overpotential at electrode–electrolyte interfaces. *J. Electroanal. Chem.* **2022**, *907*, 116079. [CrossRef]
11. Tasnim, S.; Du, Y.; Rahman, M.E.; Ahmadi, R.B.; Doh, S.I. Effect of using palm oil fuel ash on the durability of cement paste in ammonium nitrate solution. *Constr. Build. Mater.* **2020**, *257*, 119597. [CrossRef]
12. Liu, H.; Shi, N.; Han, K.; Fu, X.; Fang, Y. Study on the Attack of Concrete by External Sulfate under Electric Fields. *Coatings* **2024**, *14*, 1008. [CrossRef]
13. Zhang, K.; Lin, W.; Zhang, Q.; Wang, D.; Luo, S. Evaluation of anisotropy and statistical parameters of compressive strength for 3D printed concrete. *Constr. Build. Mater.* **2024**, *440*, 137417. [CrossRef]
14. Nagajothi, S.; Elavenil, S. Effect of GGBS Addition on Reactivity and Microstructure Properties of Ambient Cured Fly Ash Based Geopolymer Concrete. *Silicon* **2020**, *13*, 507–516. [CrossRef]
15. Ding, T.; Xiao, J.; Zou, S.; Wang, Y. Hardened properties of layered 3D printed concrete with recycled sand. *Cem. Concr. Compos.* **2020**, *113*, 103724. [CrossRef]
16. Duan, Z.; Li, L.; Yao, Q.; Zou, S.; Singh, A.; Yang, H. Effect of metakaolin on the fresh and hardened properties of 3D printed cementitious composite. *Constr. Build. Mater.* **2022**, *350*, 128808. [CrossRef]
17. Hoshi, Y.; Soukura, M.; Shitanda, I.; Itagaki, M.; Kato, Y. Corrosion Monitoring of Reinforcing Steel in Concrete By Electrochemical Impedance Spectroscopy. *ECS Meet. Abstr.* **2020**, *MA2015-01*, 1083. [CrossRef]
18. Ma, H.; Li, Z.; Chen, E.; Yu, H.; Tan, Y.; Wu, C.; Han, X. Research on the corrosion behavior of rebar in basic magnesium sulfate cement concrete based on the electrochemical impedance spectroscopy method. *Constr. Build. Mater.* **2025**, *466*, 140326. [CrossRef]
19. Madej, D. A new implementation of electrochemical impedance spectroscopy (EIS) and other methods to monitor the progress of hydration of strontium monoaluminate ($SrAl_2O_4$) cement. *J. Therm. Anal. Calorim.* **2019**, *139*, 17–28. [CrossRef]
20. Bortoletto, M.; Sanches, A.; Santos, J.; da Silva, R.; Tashima, M.; Payá, J.; Soriano, L.; Borrachero, M.; Malmonge, J.; Akasaki, J. New insights on understanding the Portland cement hydration using electrical impedance spectroscopy. *Constr. Build. Mater.* **2023**, *407*, 133566. [CrossRef]
21. Chi, L.; Wang, M.; Wang, Z.; Li, Z.; Peng, B.; Li, J. Nondestructive Monitoring Hydration of Belite Calcium Sulfoaluminate Cement by EIS Measurement. *Materials* **2022**, *15*, 4433. [CrossRef]
22. Gao, F.; Cheng, L.; Liu, J.; Zhu, J. Non-Destructive Monitoring of Hydration Characteristics in Alternative Materials and Seawater-Based Cementitious Pastes Using Electrochemical Impedance Spectroscopy. *Sustainability* **2024**, *16*, 7368. [CrossRef]
23. Liu, G.; Zhang, Y.; Ni, Z.; Huang, R. Corrosion behavior of steel submitted to chloride and sulphate ions in simulated concrete pore solution. *Constr. Build. Mater.* **2016**, *115*, 1–5. [CrossRef]
24. Qian, C.; Zhou, S.; Zhang, Z.; Zhu, Y. Effect of nano-SiO_2 on sulfate attack resistance of cement pastes by electrochemical impedance spectroscopy. *J. Build. Eng.* **2023**, *72*, 106742. [CrossRef]
25. Taborda-Llano, I.; Hoyos-Montilla, A.A.; Asensio, E.; Guerrero, A.M.; Tobón, J.I. Influence of the construction process parameters on the mechanical performance and durability of 3D printed concrete (3DPC): A systematic review. *J. Build. Eng.* **2025**, *118*, 114965. [CrossRef]

26. Ler, K.-H.; Ma, C.-K.; Chin, C.-L.; Ibrahim, I.S.; Padil, K.H.; Ab Ghafar, M.A.I.; Lenya, A.A. Porosity and durability tests on 3D printing concrete: A review. *Constr. Build. Mater.* **2024**, *446*, 137973. [CrossRef]
27. Rui, A.; Wang, L.; Lin, W.; Ma, G. Experimental study on damage anisotropy of 3D-printed concrete exposed to sulfate attack. *Constr. Build. Mater.* **2023**, *407*, 133590. [CrossRef]
28. Nodehi, M.; Aguayo, F.; Nodehi, S.E.; Gholampour, A.; Ozbakkaloglu, T.; Gencel, O. Durability properties of 3D printed concrete (3DPC). *Autom. Constr.* **2022**, *142*, 104479. [CrossRef]
29. Hu, J.; Liu, Y.; Dong, Z.; Zhang, S. A novel method to measure the actual corrosion resistance/rate of steel reinforcement during impressed-current accelerated corrosion test. *Constr. Build. Mater.* **2024**, *426*, 136060. [CrossRef]
30. Melara, E.K.; Mendes, A.Z.; Andreczevecz, N.C.; Bragança, M.O.; Carrera, G.T.; Medeiros-Junior, R.A. Monitoring by electrochemical impedance spectroscopy of mortars subjected to ingress and extraction of chloride ions. *Constr. Build. Mater.* **2020**, *242*, 118001. [CrossRef]
31. Wu, H.; Huang, Y.; Liu, S.; Liu, Y.; Liu, T.; Zuo, B.; Li, S. Electrochemical Degradation Mechanism of Desert Sand Concrete Under the Combined Action of Electric Field and Sulfate. *Sustainability* **2025**, *18*, 176. [CrossRef]
32. Xu, A.; Weng, Y.; Zhao, R. Permeability and Equivalent Circuit Model of Ionically Conductive Mortar Using Electrochemical Workstation. *Materials* **2020**, *13*, 1179. [CrossRef]
33. *GB/T 17671-2021*; Method of Testing Cements—Determination of Strength. China Building Materials Federation: Beijing, China, 2021. Available online: https://std.samr.gov.cn/gb/search/gbDetailed?id=71F772D798CCD3A7E05397BE0A0AB82A (accessed on 15 May 2025).
34. Huang, Q.; Wang, C.; Zeng, Q.; Yang, C.; Luo, C.; Yang, K. Deterioration of mortars exposed to sulfate attack under electrical field. *Constr. Build. Mater.* **2016**, *117*, 121–128. [CrossRef]
35. Li, C.; Li, J.; Ren, Q.; Zhao, Y.; Jiang, Z. Degradation mechanism of blended cement pastes in sulfate-bearing environments under applied electric fields: Sulfate attack vs. decalcification. *Compos. Part B Eng.* **2022**, *246*, 110255. [CrossRef]
36. Irassar, E.F. Sulfate attack on cementitious materials containing limestone filler—A review. *Cem. Concr. Res.* **2009**, *39*, 241–254. [CrossRef]
37. Chung, S.-Y.; Kim, J.-S.; Lehmann, C.; Stephan, D.; Han, T.-S.; Elrahman, M.A. Investigation of phase composition and microstructure of foamed cement paste with different supplementary cementing materials. *Cem. Concr. Compos.* **2020**, *109*, 103560. [CrossRef]
38. Li, G.; Wang, B.; Panesar, D.K.; Chen, Q. Electrochemical impedance spectroscopy: Effects of stray current and sulfate exposure on rubber powder mortar. *Cem. Concr. Compos.* **2024**, *152*, 105615. [CrossRef]
39. Yu, Z.; Zhao, Y.; Ba, H.; Liu, M. Relationship between buck electrical resistivity and drying shrinkage in cement paste containing expansive agent and mineral admixtures. *J. Build. Eng.* **2021**, *39*, 102261. [CrossRef]
40. Jindal, B.B. Investigations on the properties of geopolymer mortar and concrete with mineral admixtures: A review. *Constr. Build. Mater.* **2019**, *227*, 116644. [CrossRef]
41. He, R.; Ma, H.; Hafiz, R.B.; Fu, C.; Jin, X.; He, J. Determining porosity and pore network connectivity of cement-based materials by a modified non-contact electrical resistivity measurement: Experiment and theory. *Mater. Des.* **2018**, *156*, 82–92. [CrossRef]
42. Salcedo, I.R.; Cuesta, A.; Shirani, S.; León-Reina, L.; Aranda, M.A.G. Accuracy in Cement Hydration Investigations: Combined X-ray Microtomography and Powder Diffraction Analyses. *Materials* **2021**, *14*, 6953. [CrossRef]
43. Escalante-García, J.I.; Sharp, J.H. The microstructure and mechanical properties of blended cements hydrated at various temperatures. *Cem. Concr. Res.* **2001**, *31*, 695–702. [CrossRef]
44. Wang, Y.; Lei, L.; Liu, J.; Ma, Y.; Liu, Y.; Xiao, Z.; Shi, C. Accelerators for normal concrete: A critical review on hydration, microstructure and properties of cement-based materials. *Cem. Concr. Compos.* **2022**, *134*, 104762. [CrossRef]
45. Zhao, G.; Li, J.; Han, F.; Shi, M.; Fan, H. Sulfate-induced degradation of cast-in-situ concrete influenced by magnesium. *Constr. Build. Mater.* **2018**, *199*, 194–206. [CrossRef]
46. John, E.; Stephan, D. Calcium silicate hydrate—In-situ development of the silicate structure followed by infrared spectroscopy. *J. Am. Ceram. Soc.* **2021**, *104*, 6611–6624. [CrossRef]
47. Li, S.; Huang, Y.; Cui, Q.; Bai, R.; Li, H.; Jiao, L. Effect of calcium content on geopolymer consolidation of saline soils in the seasonally frozen zone. *Sci. Rep.* **2025**, *15*, 16168. [CrossRef] [PubMed]
48. Shao, W.; Xiao, Q.; Zhang, W.; Shi, D. Numerical modeling of chloride convection-diffusion-reaction in reinforced concrete under external sulfate attack and drying-wetting cycles. *Constr. Build. Mater.* **2025**, *472*, 140964. [CrossRef]
49. Henning, R.; Sturm, P.; Geddes, D.A.; Keßler, S.; Walkley, B.; Gluth, G.J.G. The influence of curing temperature on the strength and phase assemblage of hybrid cements based on GGBFS/FA blends. *Front. Mater.* **2022**, *9*, 982568. [CrossRef]
50. Elahi, M.M.A.; Shearer, C.R.; Reza, A.N.R.; Saha, A.K.; Khan, N.N.; Hossain, M.; Sarker, P.K. Improving the sulfate attack resistance of concrete by using supplementary cementitious materials (SCMs): A review. *Constr. Build. Mater.* **2021**, *281*, 122628. [CrossRef]

51. Wang, D.; Zhang, Y.; Liu, C.; Liu, Z. A mechanistic model of the degradation of cement-based materials subjected to sulfate attack. *Constr. Build. Mater.* **2024**, *421*, 135654. [CrossRef]
52. Ma, F.; Chen, L.; Lin, Z.; Liu, Z.; Zhang, W.; Guo, R. Microstructure and Key Properties of Phosphogypsum-Red Mud-Slag Composite Cementitious Materials. *Materials* **2022**, *15*, 6096. [CrossRef] [PubMed]
53. Feng, P.; Liu, J.; She, W.; Hong, J. A model investigation of the mechanisms of external sulfate attack on portland cement binders. *Constr. Build. Mater.* **2018**, *175*, 629–642. [CrossRef]

Disclaimer/Publisher's Note: The statements, opinions and data contained in all publications are solely those of the individual author(s) and contributor(s) and not of MDPI and/or the editor(s). MDPI and/or the editor(s) disclaim responsibility for any injury to people or property resulting from any ideas, methods, instructions or products referred to in the content.